

Analysis of the 12 April 2020 Northern Louisiana Tornadic QLCS

TODD A. MURPHY, TESSA M. STETZER, LAUREN WALKER, & TYLER FRICKER
University of Louisiana Monroe, Monroe, LA

BRAD BRYANT & CHARLES WOODRUM
NOAA/National Weather Service, Shreveport, LA

(Manuscript received 13 September 2021; review completed 6 June 2022)

ABSTRACT

On 12 April 2020, a tornadic quasi-linear convective system (QLCS) produced two EF-3 tornadoes in Ouachita Parish, Louisiana in close proximity to instrumentation operated by the University of Louisiana Monroe's (ULM) Atmospheric Science program. In addition to the in situ environmental information, a high-resolution aerial damage survey was conducted by the ULM Unmanned Aerial Systems program. In this paper, these datasets are used to provide a comprehensive environmental and storm-scale analysis of the tornadic QLCS through northern Louisiana. In addition, we discuss the importance of aerial damage surveys, and how Doppler radar-derived tornado intensity estimates compared to the damage survey.

1. Introduction

A multi-day outbreak of severe weather occurred in the United States on 12 April–13 April 2020, with the bulk of severe storm reports occurring on 12 April 2020 (Easter Sunday) in the southeastern United States. A total of 140 tornadoes were surveyed (Fig. 1), including 35 that were EF-2 or stronger. Additionally, 38 fatalities were reported (32 due to tornadoes), making this tornado outbreak one of the largest and deadliest in recent history. Among the tornadoes, three occurred in Ouachita Parish in northeastern Louisiana as a quasi-linear convective system (QLCS) moved along the I-20 corridor during the morning and early afternoon of 12 April 2020. Of particular interest is an EF-3 tornado that tracked through Monroe, Louisiana, the urban and economic hub of the region, and an additional EF-3 tornado that developed at nearly the same time approximately 13 km north of Monroe, near Sterlington, Louisiana. Although no casualties (injuries + fatalities) were reported, over 450 homes across the paths were impacted; 23 homes were destroyed and 108 incurred major damage. Several industrial areas were also damaged, most noteworthy being the Monroe

Regional Airport (KMLU), where an estimated \$25-30 million (M) in damage occurred.

This event is scientifically interesting due to the rich environmental and storm-scale data collected by the University of Louisiana Monroe's (ULM) Atmospheric Science program's instrumentation. The Monroe EF-3 tornado tracked within close range to the polarimetric S-band Doppler weather radar operated by ULM (KULM; Murphy et al. 2019) (Fig. 2); at one point the circulation was <1.0 km from the radar. The circulation passed within 300 m of the Automated Surface Observing Systems (ASOS) site at KMLU. In addition, ULM's microwave radiometer (MWR) and Doppler wind lidar (DWL) collected data during the event, all close (<1.0 to 5.0 km) to the QLCS and the Monroe tornado. Personnel from ULM's Unmanned Aircraft Systems (UAS) program conducted UAS flights of both EF-3 tornado tracks, collecting high-resolution georeferenced imagery of the damage paths. Additional aerial imagery was collected by the Ouachita Parish Governor's Office of Homeland Security and Emergency Preparedness (GOHSEP), and ground surveys were completed by the authors. In total, this enabled the creation of a high-resolution damage

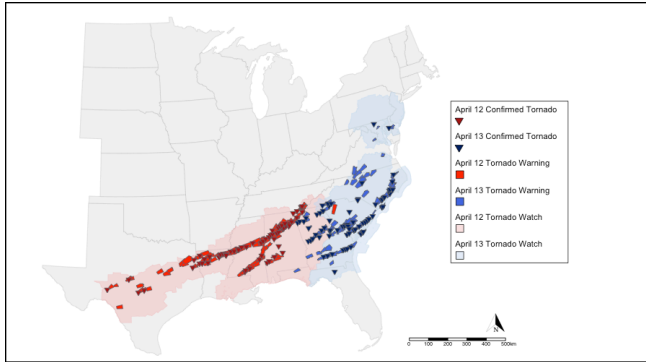


Figure 1. Tornado watches, warnings, and confirmed tornadoes during the 12–13 April 2020 severe weather event. *Click image for an external version; this applies to all figures and hereafter.*

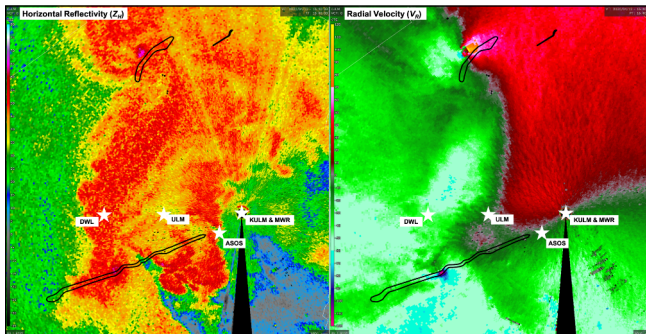


Figure 2. 1.8° horizontal reflectivity (left; dBz) and radial velocity (right; kts) from KULM valid 1640 UTC 12 April 2020. Tornado tracks for the three Ouachita Parish tornadoes are outlined in black. The southern circulation produced the EF-3 tornado through Monroe, LA and the northern circulation produced the EF-3 tornado and a weaker EF-1 tornado near Sterlington, LA. Locations of instruments are noted by the stars and labels. The distance between KULM and the DWL is approximately 10.5 km. *Click the image for an animation at 0.4° valid 1632–1649 UTC.*

survey to complement the official National Weather Service (NWS) Shreveport (SHV) survey.

Current QLCS tornado knowledge has been shaped by observational and modeling studies (e.g., Rotunno et al. 1988; Weisman and Trapp 2003; Trapp and Weisman 2003; Wheatley and Trapp 2008; Atkins and St. Laurent 2009; Schenkman et al. 2012; Smith et al. 2012; Thompson et al. 2012; Sherburn and Parker 2014; Sherburn et al. 2016). Using past work that shows an importance of line-relative shear and cold pool strength, Schaumann and Przybylinski (2012) developed the “Three Ingredients Method” (3IM), an

operationally based nowcasting technique used to anticipate QLCS mesovortexgenesis and tornadogenesis (Gibbs 2021). However, QLCS tornadoes remain a significant operational forecasting and nowcasting challenge, in part because of knowledge gaps in our understanding of processes that lead to QLCS tornadogenesis or how such processes are linked to the near-storm environment of the QLCS. These gaps are due to a lack of quality QLCS observations, the small size and transient nature of most QLCS tornadoes, and the fact that most QLCS tornadoes are weak (Trapp et al. 2005). This is problematic when one considers (1) a high percentage of tornadoes in the southeastern United States are produced by QLCSs (Ashley et al. 2019) and (2) these tornadoes exhibit lower tornado warning performance metrics (i.e., a low probability of detection, high false alarm rate, and less warning lead time) compared to supercellular tornadoes (Brotzge et al. 2013; Anderson-Frey et al. 2019; Gibbs and Bowers 2019). A primary motivation of this paper is to contribute to current QLCS tornado knowledge by utilizing the rich ULM datasets, augmented by additional NOAA/NWS observations (e.g., radiosonde, ASOS, etc.), to provide an environmental and storm-scale analysis of an unusual EF-3 producing tornadic QLCS through northern Louisiana and Ouachita Parish.

The combination of the high-resolution damage survey and the close tracking of the Monroe tornado to KULM also presents a unique opportunity to compare the Doppler radar data to tornado track damage and intensity. Much work has been and continues to be done on correlating tornado intensity and size to Doppler radar measurements (e.g., Wurman and Alexander 2005; Wurman et al. 2007; Toth et al. 2013; Wurman et al. 2013; Van Den Broeke and Jauernic 2014; Bodine et al. 2014; Kingfield and LaDue 2015; Van Den Broeke 2017). Others have included environmental information, such as environmental wind shear, to bound the radar-based tornado intensity estimates (e.g., Smith et al. 2015; Thompson et al. 2017; Cohen et al. 2018). Despite our evolution in understanding thanks to advancing radar technology, gaps in the radar network and incomplete damage surveys have slowed progress. There is significant operational value in improving radar-derived tornado intensity estimates because it can allow the NWS to issue more confident warnings utilizing specific, impact-based wording (Gibbs 2016; Bentley et al. 2021).

A secondary motivation of this paper is to share details and discuss the importance of the enhanced damage survey, including how the survey compares with the official NWS survey and to radar-derived intensity estimates. In addition, the enhanced damage survey characteristics are evaluated and applied to a predictive casualty model as a means of providing an estimated casualty rate for the Monroe EF-3 tornado. Similar to previous work on the prediction of tornado casualty events (Simmons and Sutter 2008, 2011; Lim et al. 2017; Fricker et al. 2017; Elsner et al. 2018; Fricker and Elsner 2019), this model establishes an expected casualty rate (i.e., the number of casualties per tornado) for the Monroe EF-3 tornado given its individual damage characteristics. With this number established, differences in the observed and expected casualty outcomes are evaluated through a value of statistical life that stands as a possible economic savings of reduced casualties (Cho and Kurdzo 2019).

2. Data and methods

The environmental data for this study were derived from instruments operated by the ULM Atmospheric Science program described in Table 1 and complementary data from other NOAA/NWS sources such as NEXRAD, ASOS, radiosonde, and mesoscale analysis datasets. KULM is a polarimetric S-band radar with specifications similar to the NEXRADs; more information on KULM is provided in Murphy et al. (2019). KULM was operating in its “fast” volume scan mode, providing new radar data at 0.4°, 0.9°, 1.8°, and 3.0° elevation angles every 60 s. The Monroe tornado tracked within extreme close range to KULM, forming ~16 km to the southwest and moving <1.0 km south of the radar during its lifecycle. Based on the scanning strategy, the range of minimum heights sampled are estimated at 175 m AGL (at 16 km range) to 40 m AGL (at 1.0 km range) based on standard atmospheric refraction. At this range, sidelobe contamination is possible and may skew the interpretation of the sampled heights. The radar data were evaluated in the Gibson Ridge GR2Analyst (GR2A) software (http://grlevelx.com/gr2analyst_2/). In some instances, the GR2A de-aliasing algorithm failed, so radial velocities (V_R) were manually de-aliased using the National Center for Atmospheric Research (NCAR) solo3 software to obtain accurate V_R values.

The ULM DWL is a pulsed scanning Doppler lidar manufactured by Halo Photonics (model Streamline

XR). The DWL is sensitive to atmospheric aerosols with a maximum possible range up to 12 km AGL; in practice, the actual range is 1.5–3.0 km AGL based on boundary layer aerosol loading. Optically thick cloud cover and precipitation attenuates the signal. The DWL has an all-sky scanner, enabling scans from 0° to 360° in azimuth and –15° to 195° in elevation. For this event, the DWL collected vertical stares (90° elevation) up to 2 km AGL of attenuated backscatter (β ; $\text{m}^{-1} \text{sr}^{-1}$), signal-to-noise ratio (SNR), and vertical velocity (w ; m s^{-1}), and 6-point 70° elevation velocity-azimuth display (VAD) scans every 10 min to derive horizontal wind profiles. The first range gate is sampled at approximately 60 m AGL, and range gate spacing is 18 m. DWL data were thresholded on $\text{SNR} < 0.01$ to remove noise and to otherwise assure valid data (Päschke et al. 2015); this generally removes data in weak signal return. VAD wind profiles (VWP) were used only where the VAD retrieval error was low. DWL data are used in this study to assess kinematic trends in the boundary layer as the tornadic QLCS approached Monroe. Similarly, VWPs derived from the KSHV WSR-88D data were used to assess kinematic trends as the QLCS approached Shreveport, Louisiana.

The ULM MWR measures downwelling microwave radiance in 35 calibrated channels and uses an artificial neural network to derive atmospheric profiles of temperature, water vapor, and liquid water from sky brightness temperatures in the oxygen and water vapor absorption bands. Profiles are retrieved approximately every 2 min from the surface to 10 km AGL, with the greatest resolution and accuracy in the lowest 3 km AGL. MWR data are negatively affected by precipitation, so profiles are quality controlled to remove those when rain was present. The data were then averaged using a rolling 10-min averaging window to remove noise. MWR data are used in this study to assess thermodynamic trends in the boundary layer (specifically the 0–1-km lapse rate) as the tornadic QLCS approached Monroe. Figure 2 shows the locations of the ULM instrumentation relative to the tornado track and circulation.

To construct the high-resolution damage survey, UAS flights over the damage path were conducted within days of the event using a Yuneec H520 hexacopter with an attached E90 20-megapixel camera. This allowed the collection of high-resolution georeferenced aerial imagery. The UAS imagery was processed using the Pix4Dmapper software to create high-resolution orthomosaic GeoTiffs and kml files for

Table 1. ULM Atmospheric Science instrument operating specifications on 12 April 2020.

Instrument	Description	Quantities Measured/ Calculated	Measurement Height	Spatial Resolution	Temporal Resolution
KULM	10.162 cm wavelength (S-band), 1100 Hz PRF, 0.93° beam width, dual-polarization (STAR)	horizontal reflectivity factor (Z_H), radial velocity (V_R), spectrum width (SW), differential reflectivity (Z_{DR}), correlation coefficient (CC), differential propagation phase (Φ_{DP})	4 elevation angles (0.4°, 0.9°, 1.8°, 3.0°)	125 m gate width	60-s volume update
Doppler wind lidar (DWL)	pulsed all-sky scanner, 1.5 μ m wavelength	signal-to-noise ratio (SNR), attenuated backscatter (β), V_R , horizontal (u , v) and vertical (w) motion	~60 m - 12 km (up to 2 km in this study)	Selectable 18 - 120 m (18 m in this study)	0.1 - 10 Hz (2 Hz in this study)
Microwave Radiometer (MWR)	measures downwelling radiance in 35-calibrated channels	temperature, water vapor, and liquid water profiles; integrated values of water vapor and cloud water	surface - 10 km	50 m up to 500 m, 100 m up to 2 km, 250 m above 2 km	~2-min

viewing in Google Earth. The processed UAS imagery, along with aerial imagery provided by GOHSEP, and other ground imagery from the NWS SHV survey and a personal ground survey by author Murphy, were analyzed independently by three of the authors (Murphy, Stetzer, and Walker) using the EF toolkit (LaDue and Mahoney 2006) to assign damage ratings to most structures and some trees along the probable tornado path. A consensus EF rating for structures was determined from the three independent surveys. We also consulted with authors Bryant and Woodrum when there were uncertainties surrounding damage indicators and the degree of damage.

The American Society for Civil Engineers' (ASCE) Wind Speed Estimation Standards Committee (WSE) has been developing revised tree damage indicators (DIs) to better assess tornado intensity in wooded areas (LaDue 2016; LaDue et al. 2018). The revised method will include the percent of tree falls observed along the tornado path to estimate intensity, as in Godfrey and Peterson (2017) (C. Godfrey and C. Peterson, personal communication) (Table 2). This revision will better align the United States EF-scale with the Canadian EF-scale (Environment Canada 2022). The official NWS SHV survey of the tornadoes in this study included several wooded areas they were unable to investigate due to a lack of roads and areas that were blocked by waterways. In these areas, the UAS imagery were used for a complete tree fall analyses similar to Godfrey and

Peterson (2017), but using the draft multi-tree DI to assign wind speed estimates (Table 2). In the wooded areas, the imagery was divided into 10 000 m² boxes centered along the tornado track. The number of trees in each box were counted, and then marked as either undisturbed, snapped/uprooted, or indeterminate. If the tree was snapped/uprooted, then the fall direction was also noted. The percent of trees either snapped or uprooted was determined in each box and a wind speed estimate and EF-rating for each box was reached based on Table 2. Indeterminate trees were ultimately included in the undisturbed category for determining the tree fall percentage. Consultations with C. Godfrey and C. Peterson (personal communication) helped refine our understanding of tree/forest resistance levels.

The casualty model relies on detailed spatial damage characteristics found through the high-resolution ULM damage survey. In particular, the model includes estimates of population density, energy dissipation, the number of mobile homes, and year, month, and hour of occurrence. Energy dissipation (power) is estimated as the product of tornado path area and the cube of the wind field (Fricker et al. 2014) and population density and the number of mobile homes is estimated using a dasymetric method (Fricker 2020a) with underlying demographic information from 2019 American Community Survey 5-year estimates. The modeling framework is based on recent regression

Table 2. Estimated wind speeds (mph) required to uproot/snap multiple trees in a heavily wooded area based on tree/forest resistance and percent of trees snapped or uprooted in a 10 000 m² area. Values are from a proposed revision to the tree DI in the U.S. EF Scale (C. Godfrey and C. Peterson, 2021, personal communication).

Damage Description	Estimated Wind Speed (rounded to nearest 5 mph)		
	Below Normal Resistance	Normal Resistance	Above Normal Resistance
Small limbs (<2" diameter) broken	35	45	55
Large limbs (≥2" diameter) broken	40	55	70
Up to 25% of large trees snapped or uprooted	50	70	95
≥25–49% of large trees snapped or uprooted	65	95	120
≥50–74% of large trees snapped or uprooted	90	120	145
≥75% of large trees snapped or uprooted; numerous trees may be stubbed, with only stubs of large limbs remaining	120	145	170
Bodily removal of >20% of trees from substrate	130	170	210

analyses (Fricker et al. 2017; Elsner et al. 2018; Fricker and Elsner 2019) and formally described below.

3. Environment and storm-scale analysis

The tornado event on 12–13 April 2020 was a synoptically evident severe event that was anticipated at least a week prior. The Storm Prediction Center's (SPC) Day 4–8 Convective Outlook issued 5 April 2020 mentioned “strong to severe storms” across the southeastern United States for the Day 8 period, and the region was included in a broad 15% probability area on the Day 5 outlook issued 8 April 2020 (Fig. 3a). A Moderate Risk for severe convective storms was issued by Day 3, and this remained largely unchanged during subsequent updates (Fig. 3c,d). Synoptically, the event was driven by an upper-tropospheric shortwave trough that took on a neutral to negative tilt as it ejected east-northeastward across the southern Plains and lower Mississippi Valley (Fig. 4). The response from the upper-level dynamics included surface cyclogenesis (Fig. 5) and low-level moisture advection inland from the Gulf of Mexico (Fig. 5 & 6) in conjunction with a 25.7–36.0-m s⁻¹ (50–70-kt) southerly low-level jet (Figs. 4 and 7) that developed by mid-morning to early afternoon across the Deep South. The 850-mb wind at Jackson, Mississippi (JAN) increased from 19 m s⁻¹ (37 kts) at 12 UTC to 34 m s⁻¹ (66 kts) at 18 UTC (Fig. 7b,d). A warm front advanced northward during the mid-morning (Fig. 5), and by 15 UTC, dewpoint temperatures exceeded 18.3°C (65°F) along the I-20

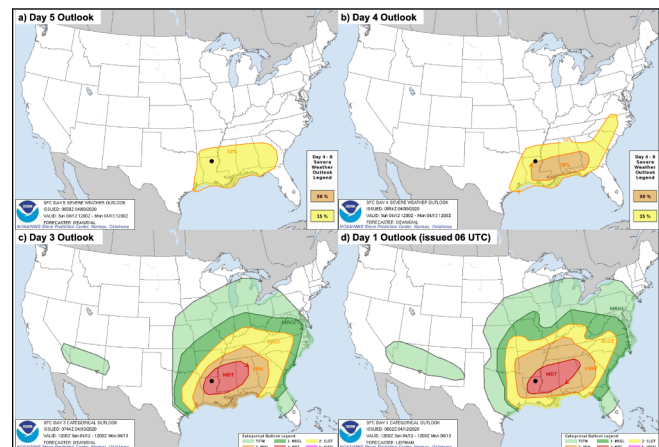


Figure 3. Storm Prediction Center's Severe Weather and Categorical Outlooks valid 12 UTC 12 April 2020 – 12 UTC 13 April 2020 issued at (a) Day 5, (b) Day 4, (c) Day 3, and (d) 06 UTC Day 1. The black dot is the approximate location of Ouachita Parish, LA.

corridor across northern Louisiana and central Mississippi, and 21.1°C (70°F) to the south (Figs. 5c).

Multiple elevated convective clusters were ongoing across western and central Texas (TX) as early as 06 UTC in response to the lead shortwave trough and low-to mid-tropospheric warm air advection (Figs. 4a,b). This convection grew upscale, becoming better organized ahead of a 25.7–36.0-m s⁻¹ (50–70-kt) westerly midlevel jet (Figs. 4a,b & 7a,b), and establishing a mature cold pool by 09–12 UTC as it approached Louisiana (Figs. 5a, b). This convection was further supported by elevated moderate-to-strong

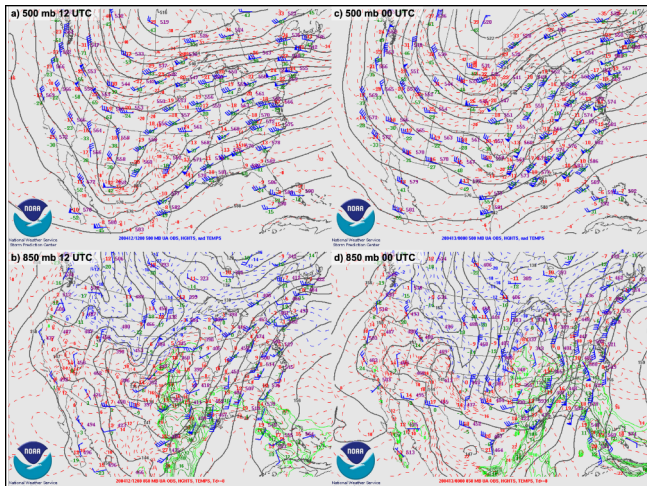


Figure 4. Upper-air charts from the Storm Prediction Center valid 12 UTC 12 April 2020 at (a) 500-mb and (b) 850-mb and charts valid 00 UTC 13 April 2020 at (c) 500-mb and (d) 850-mb. Black contours are geopotential heights (dm), dashed red contours are temperature ($^{\circ}\text{C}$), and green contours are dewpoint ($^{\circ}\text{C}$). On (b) and (d) temperatures $\leq 0^{\circ}\text{C}$ are plotted using dashed blue contours. Blue wind barbs indicate the wind speed (kts) and direction at each level.

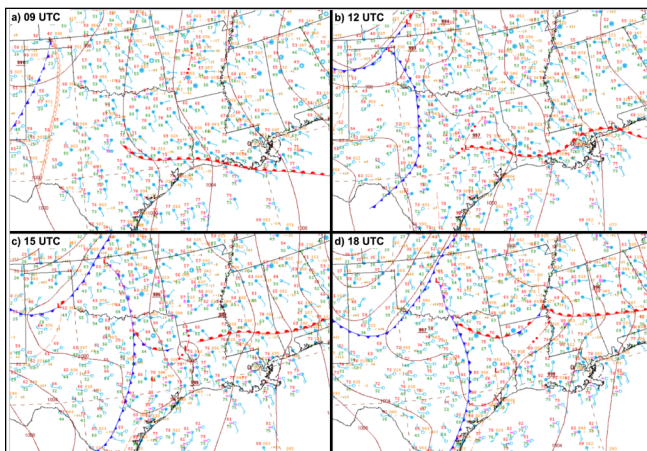


Figure 5. Surface analyses from the Weather Prediction Center valid (a) 09, (b) 12, (c) 15, and (d) 18 UTC 12 April 2020. Station models and surface boundaries are given using standard notation. Black contours are mean sea level pressure (mb).

convective available potential energy (CAPE) located above an 800-mb capping inversion; the most unstable CAPE on the 12 UTC SHV sounding was $>2500 \text{ J kg}^{-1}$ (Fig. 7a; Table 3). The inversion, and a relatively cooler and drier boundary layer towards the east, prevented the convection from becoming surface-based until a few

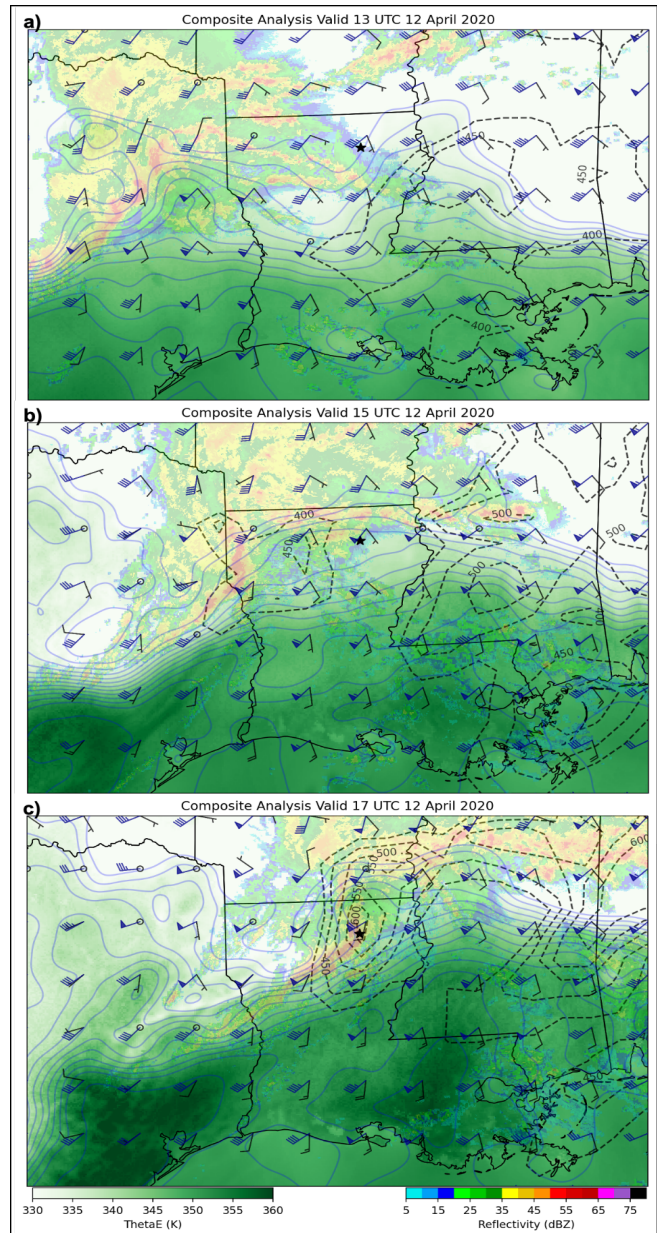


Figure 6. Reflectivity (dBZ), 0–1-km storm relative helicity (SRH; dashed black contours; $\text{m}^2 \text{ s}^{-2}$), surface equivalent potential temperature (ThetaE; green shading and solid blue contours; K), surface wind (black barbs; kts), and 3 km shear vector (dark blue barbs; kts) valid (a) 13 UTC, (b) 15 UTC, and (c) 17 UTC 12 April 2020. ThetaE is contoured in 2 K increments beginning at 330 K. SRH is contoured in 50 $\text{m}^2 \text{ s}^{-2}$ increments beginning at 400 $\text{m}^2 \text{ s}^{-2}$. Surface ThetaE and winds are derived from the 2.5 km resolution Real Time Mesoscale Analysis (RTMA). 0–1-km SRH and 3-km shear vector are from the SPC Mesoanalysis. The black star represents the location of Monroe, LA. Click the image for an hourly animation from 12–18 UTC.

Table 3. Thermodynamic and kinematic indices from the sounding data given in Fig. 7.

Index	SHV 12 UTC (Fig. 7a)	JAN 12 UTC (Fig. 7b)	SHV 18 UTC (Fig. 7c)	JAN 18 UTC (Fig. 7d)
SBCAPE (CIN) (J kg ⁻¹)	506 (-353)	0 (0)	294 (-264)	908 (-148)
MLCAPE (CIN) (J kg ⁻¹)	785 (-257)	551 (-236)	186 (-329)	840 (-137)
MUCAPE (CIN) (J kg ⁻¹)	2581 (-21)	1250 (-70)	414 (-63)	927 (-116)
0–1 km SRH (m ² s ⁻²)	231	340	-313	484
0–1 km bulk shear (kts)	26	34	37	48
0–3 km SRH (m ² s ⁻²)	296	537	-411	708
0–3 km bulk shear (kts)	26	49	57	68

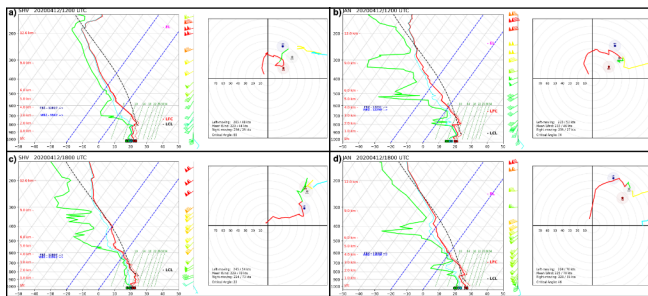


Figure 7. Sounding data plotted as a skew-t and hodograph valid 12 UTC 12 April 2020 from (a) Shreveport, LA and (b) Jackson, MS and data valid 18 UTC 12 April 2020 from (c) Shreveport, LA and (d) Jackson, MS. Images generated using the Sounding and Hodograph Analysis and Research Program in Python (SHARPPy; Blumberg et al. 2017). Relevant sounding indices are provided in Table 3.

hours later as it approached Louisiana; surface-based convective inhibition (CIN) on the 12 UTC SHV sounding was stronger than -350 J kg^{-1} (Fig. 7a; Table 3). As the aforementioned warm front lifted northward and interacted with the QLCS cold pool (marked by a tightening gradient in surface equivalent potential temperature (θ_e) [Fig. 6]), it became a focal point for a more surface-based QLCS.

Radar-derived VWP from KSHV indicated wind speeds increased immediately ahead of the QLCS near 13–14 UTC (Fig. 8a). The stronger southerly flow

contributed to the improved low-level thermodynamic environment that developed east of the convection (Fig. 6). The QLCS produced its first tornadoes at ~ 14 UTC in far northeastern Texas, near Shreveport, Louisiana, along the strengthening θ_e gradient in an increasingly favorable kinematic environment. The 12 UTC SHV sounding had 0–1-km storm-relative helicity (SRH) $>200 \text{ m}^2 \text{ s}^{-2}$ (Fig. 7a and Fig. 8b). The KSHV VWP suggests these parameters increased rapidly as the QLCS approached, with 0–1-km SRH reaching $431 \text{ m}^2 \text{ s}^{-2}$ near the time of tornado development at 14 UTC (Fig. 8b). The 0–3-km SRH increased at an even greater rate, from $296 \text{ m}^2 \text{ s}^{-2}$ on the 12 UTC sounding to $587 \text{ m}^2 \text{ s}^{-2}$ at 14 UTC (Fig. 8b). Baroclinic boundaries have been shown in past studies to augment the low-level shear (e.g., Markowski et al. 1998; Rasmussen et al. 2000; Knupp et al. 2014; Tang et al. 2016), and here the low-level flow became increasingly backed along the warm front east of the QLCS at the same time winds aloft accelerated (Fig. 8a,c).

A similar scenario was observed with the Ouachita Parish tornadoes a few hours later (Fig. 9). By 15–16 UTC, as the QLCS approached Ouachita Parish, the ULM DWL VWP showed strengthening low-level flow, with winds becoming more backed with time (Fig. 9a); near surface-to-500 m AGL hodographs lengthened and became more curved prior to the arrival of the convection (Fig. 9b). This occurred coincident with development of a meso-low at the intersection of

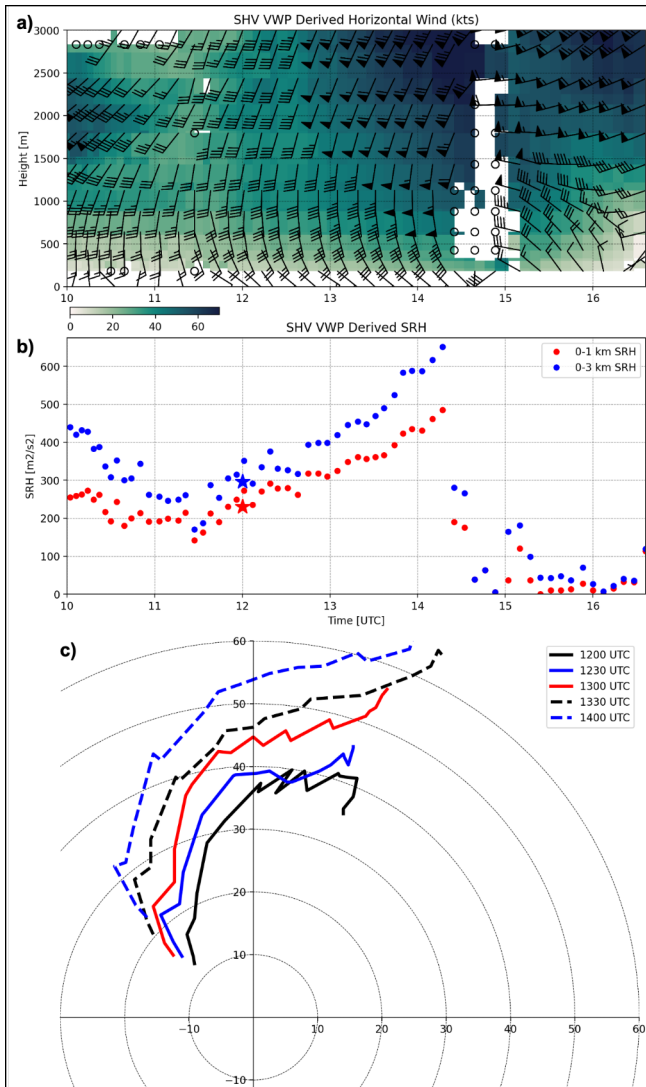


Figure 8. Time series of SHV VWP derived (a) horizontal wind (shading and wind barbs; kts) and (b) storm-relative helicity in the 1-km layer (red dots) and 3-km layer (blue dots) valid 1000–1630 UTC 12 April 2020. (c) SHV VWP-derived hodographs (kts) up to 3 km AGL at 1200 (black), 1230 (blue), 1300 (red), 1330 (black dashed), and 1400 (blue dashed) UTC. The stars in (b) represent the SRH values from the 12 UTC SHV radiosonde.

the cold pool and warm front (Fig. 5c), and further tightening of the θ_e gradient (Fig. 6). Whereas the environmental shear was more than sufficient for potentially tornadic QLCSs, 0–1-km SRH derived from the SPC Mesoanalysis indicated local maximums in SRH immediately ahead of the QLCS near areas where tornadoes developed. This was especially the case for the Ouachita Parish tornadoes, where a local maximum in 0–1-km SRH $>600 \text{ m}^2 \text{ s}^{-2}$ was analyzed on the SPC

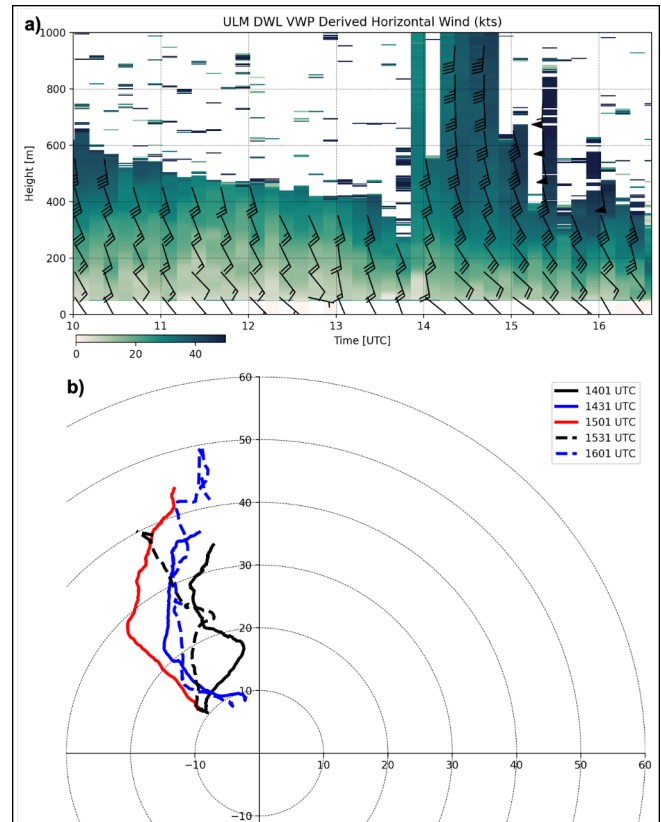


Figure 9. Time series of ULM DWL VWP-derived (a) horizontal wind (shading and wind barbs; kts) valid 1000–1630 UTC 12 April 2020. (b) ULM DWL VWP-derived hodographs (kts) up to 500 m AGL at 1401 (black), 1431 (blue), 1501 (red), 1531 (black dashed), and 1601 (blue dashed) UTC.

Mesoanalysis at 17 UTC in northeastern Louisiana (Fig. 6c). Signal attenuation prevented the ULM DWL from observing the full 0–1-km layer as the QLCS approached, but 0–500-m SRH exceeded $300 \text{ m}^2 \text{ s}^{-2}$ near 16 UTC. The 0–500-m layer (and lower) has recently come into focus as being more relevant for tornado potential (e.g., Coffey et al. 2019, 2020; Gensini et al. 2021) than deeper layers. It is possible some of the observed enhancements in wind shear were storm-induced.

A stability assessment near Monroe indicated the atmosphere became less stable as the QLCS approached (Fig. 10). RAP-derived surface-based and mean-layer CAPE (SBCAPE and MLCAPE, respectively) increased dramatically after 13 UTC, coincident with a decrease in CIN. However, CIN remained high throughout the morning because of a persistent stable layer near 850 mb on the RAP analysis. The RAP-derived 0–1-km lapse rate increased from

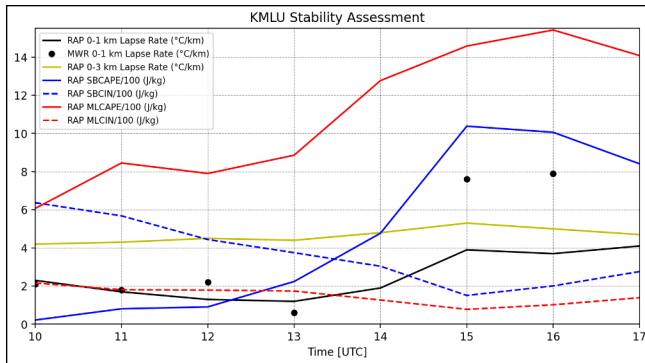


Figure 10. Time series of stability parameters derived from the RAP 00-hr analysis valid 1000–1700 UTC 12 April 2020 for Monroe, LA (KMLU). Stability parameters are 0–1-km lapse rate ($^{\circ}\text{C km}^{-1}$; solid black line), 0–3-km lapse rate ($^{\circ}\text{C km}^{-1}$; solid yellow line), surface-based CAPE (SBCAPE; J kg^{-1} ; solid blue line), surface-based CIN (SBCIN; J kg^{-1} ; dashed blue line), mean-layer CAPE (MLCAPE; J kg^{-1} ; solid red line), and mean-layer CIN (MLCIN; J kg^{-1} ; dashed red line). The CAPE and CIN values have been divided by 100 to normalize with the lapse rate values. The 0–1-km lapse rate ($^{\circ}\text{C km}^{-1}$; black dots) derived from ULM’s MWR are also given. The MWR observations near 14 and 17 UTC were excluded due to rain contamination.

near $1^{\circ}\text{C km}^{-1}$ at 12 UTC to near $4^{\circ}\text{C km}^{-1}$ at 16 UTC, all while the 0–3-km lapse rate remained relatively flat. The MWR 0–1-km lapse rate also increased, though the magnitude of increase was much greater – near $2^{\circ}\text{C km}^{-1}$ at 12 UTC to near $8^{\circ}\text{C km}^{-1}$ at 16 UTC. Recent studies on cool season QLCSs and high-shear, low-CAPE environments have shown the importance of low-level lapse rates as a tool to discriminate between significant severe and non-severe events (e.g., Sherburn and Parker 2014), and rapid destabilization near the surface commonly precedes severe events (e.g., King et al. 2017). The MWR observations suggest the RAP analysis may have underforecast the degree of near-surface destabilization preceding the convection. Such an underforecast, if correct, has implications for how operational meteorologists might anticipate the tornadic potential of QLCSs. Regardless, these observations taken together imply the boundary layer became much less stable with time as the higher θ_e air advected northward ahead of the QLCS.

The tornadic portion of the QLCS in Ouachita Parish met the operational characteristics associated with the commonly used 3IM (Warning Decision Training Division 2019) for anticipating mesovortexgenesis and QLCS tornado potential. As the

QLCS approached KULM, a well-defined, balanced updraft downdraft convergence zone (UDCZ) was observed in the horizontal reflectivity (Z_H) and V_R data, along with deep convection, a tight Z_H gradient, and bulges/bowing segments along the leading line (Fig. 11). By 16–17 UTC, the 0–3-km shear vector (dark blue wind barbs on Fig. 6) in the near-storm environment increased to $>30.9 \text{ m s}^{-1}$ (60 kts) and became nearly perpendicular to the UDCZ. The 0–3-km line normal shear is estimated at approximately $23.2\text{--}25.7 \text{ m s}^{-1}$ (45–50 kts) based on a 0–3-km shear vector of 32.4 m s^{-1} (63 kts) from 235° and a nearly north-south oriented UDCZ, well above the 15.4 m s^{-1} (30 kt) threshold required for the 3IM. In addition to meeting the 3IM criteria, several confidence builders and nudgers were present (e.g., https://www.weather.gov/media/lx/QLCS_Warnings.pdf), further increasing confidence in tornado potential.

The Monroe tornado developed on the northern end of a bowing segment in Z_H associated with a rearward V_R enhancement and within a broader cyclonic mesovortex that developed beginning 1626 UTC (Fig. 11a). An argument can be made that the line-normal shear in the vicinity of where mesovortexgenesis, and eventually tornadogenesis, occurred likely approached the full 0–3-km shear magnitude given the bowing segment would have contributed to an almost perpendicular orientation. The mesovortex became better established by 1630 UTC near the same time as a smaller area of cyclonic rotation (black circle in Fig. 11b) developed on the northern fringe of the Z_H bow. This tighter rotational velocity (V_{ROT}) signature increased in magnitude with each successive volume scan (Fig. 11c & Fig. 2 animation) until tornadogenesis at 1636 UTC. Similarly, the Sterlington EF-3 tornado developed along the northern edge of a V_R enhancement and Z_H bowing segment at 1639 UTC.

4. Tornado intensity estimates

a. Damage survey estimates

Similar intensity estimates were determined by both the NWS Shreveport ground survey and the ULM aerial survey; a maximum EF-3 intensity and small differences in the total area EF-ratings across the track (Fig. 12 and Table 5) were found between the surveys. The ULM survey provided high-resolution building-level damage assessments across portions of the track (Fig. 13), showing a large damage variability from one

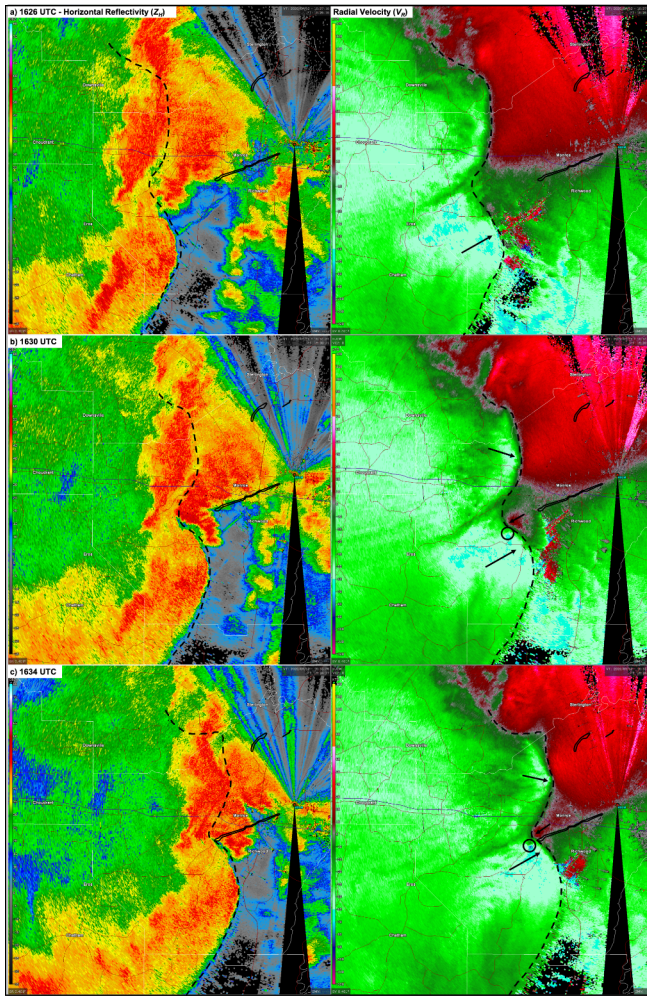


Figure 11. 0.4° horizontal reflectivity (left; dBz) and radial velocity (right; kts) from KULM valid (a) 1626, (b) 1630, and (c) 1634 UTC 12 April 2020. Tornado tracks for the three Ouachita Parish tornadoes are outlined in solid black contours. The approximate location of the updraft downdraft convergence zone is marked by the dashed black line. The black arrows represent approximate radial wind direction. The black circles in (b) and (c) represent the incipient circulation for the Monroe tornado.

structure to the next. For example, in areas with the worst damage assessments (Fig. 13b,c), EF-2 or EF-3 damage is often bordered by structures with only EF-0 damage. This materialized as residential homes with entire roofs missing and/or exterior/interior walls collapsed, adjacent to homes with only missing roof shingles. Similarly, within the Monroe Regional Airport’s industrial district (Fig. 13d), several buildings were rated EF-1 because of exterior sheet metal damage, while an aircraft hangar near the end of the

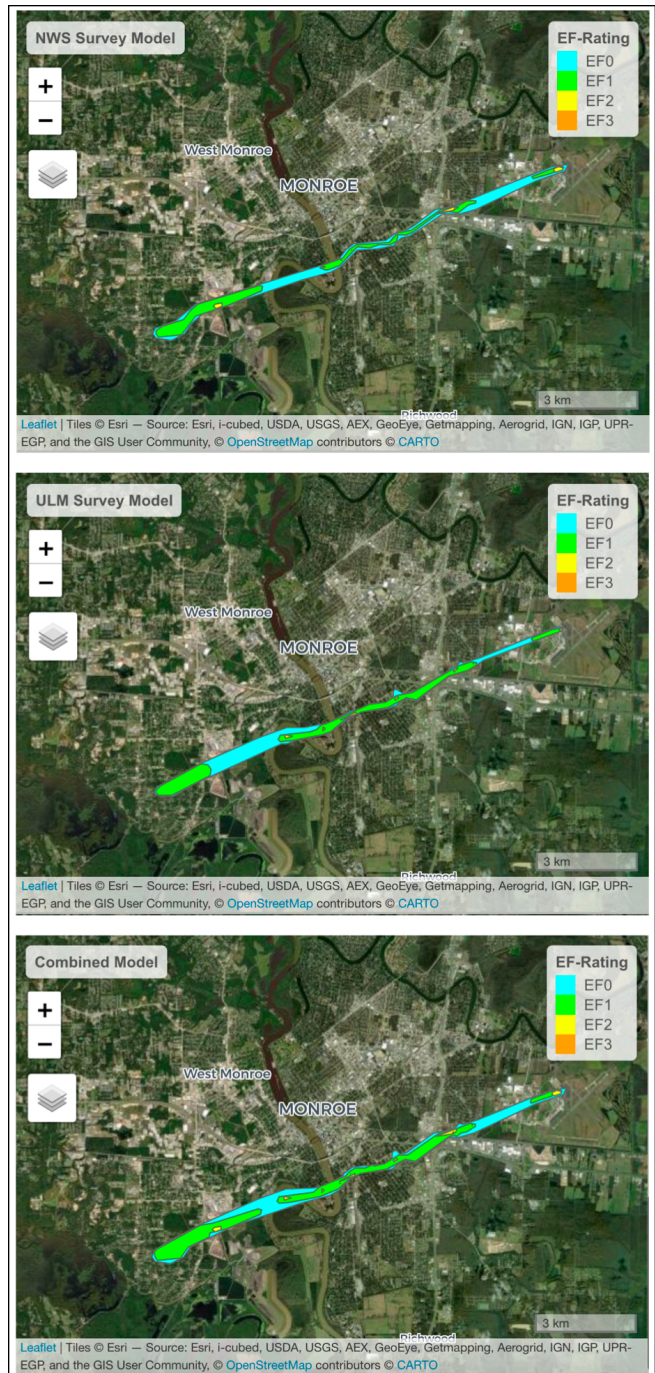


Figure 12. Damage survey assessments of the Monroe tornado from the NWS Shreveport ground survey (top), ULM aerial survey (middle), and a combined survey (bottom).

track was totally destroyed and received an EF-2 rating. Both surveys assessed a single structure, a relatively new residential single-story house, as having EF-3 damage because of a collapse of both exterior and interior walls (Fig. 13c). The ULM survey rated three

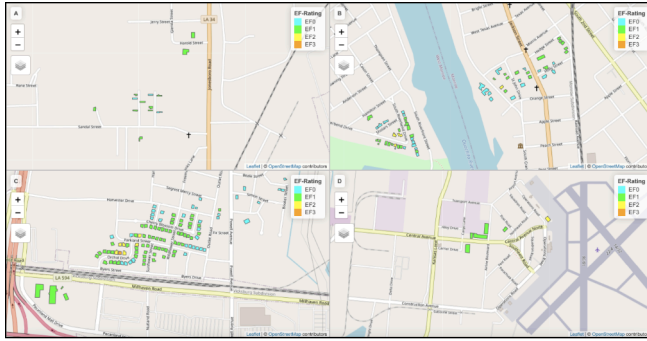


Figure 13. Building level survey information based on the ULM aerial survey.

structures as EF-2 intensity that were originally EF-1 in the NWS Shreveport survey. These structures had large sections of their roof structure removed and were located within pockets of similar damage.

The ULM survey includes a tree fall analysis for a wooded area in the path of the Monroe tornado (Fig. 14). The tree fall analysis shows two adjacent cells with >80% tree falls near the center of the tornado path, with additional surrounding cells $\geq 50\%$ tree falls. Table 4 gives intensity estimates for this area by applying the ASCE WSE proposed multi-tree DI (table 2), the Canadian EF scale tree DI, and the Godfrey and Peterson (2017) method directly. The maximum wind estimates in this area range from approximately 120 to 170 mph (EF-2 to EF-4 intensity). After consulting with leading tree fall experts (C. Godfrey and C. Peterson, personal communication), a below normal resistance level should be assumed for the intensity estimates given uncertainties surrounding the overall health of the trees and nearly saturated soil conditions. This would correspond to a below normal resistance intensity estimate of 120 mph (EF-2 intensity). Perhaps the biggest difference between the two surveys is the inclusion of EF-2 damage in this portion of the track on the ULM survey, while the NWS SHV survey was only EF-0 due to a lack of ground accessibility. To capture the full breadth of both surveys, a combined survey (Fig. 12) was generated using the maximum EF-rating along any part of the track.

A full aerial survey was not completed for the Sterlington tornado, but ULM did survey a wooded area impacted early in the tornado’s path and completed a similar tree fall analysis as above (Fig. 15). Here, significant tree falls were observed, with 7 cells having >80%, 4 cells >90%, and all but one of the analyzed cells >50% tree falls. The maximum wind estimates in this area range from approximately 120 to 224 mph

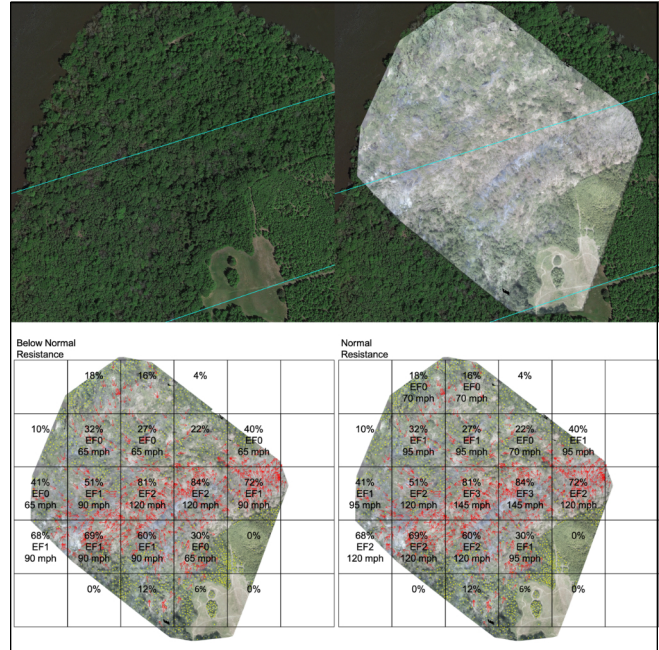


Figure 14. Before and after aerial imagery of a wooded area in the path of the Monroe tornado. The cyan lines represent the EF-0 polygon outline from the NWS Shreveport survey. Intensity estimates in 10 000 m² areas based on a tree fall analysis is provided for both below-normal tree resistance and normal tree resistance based on Table 2. Red arrows in each box represent the direction of tree fall, and yellow dots are unaffected trees. Estimates are only provided for boxes where tree falls >25% for below normal and >15% for normal resistance. Intensity estimates discussed in this paper assume below-normal resistance.

(EF-2 to EF-5 intensity), though the below normal resistance estimate is 120 mph (EF-2 intensity) (Table 4).

b. Radar estimates

As previously mentioned, the Monroe tornado moved exceptionally close to KULM allowing for an estimate of near-ground winds in the tornadic circulation based on Doppler velocities. Following past studies (e.g., Wurman and Alexander 2005; Wurman et al. 2007; Toth et al. 2013; Wurman et al. 2013), the ground-relative tornadic (V_G) wind speed during any given volume scan can be found through a vector addition of the tornado tangential velocity (V_T) and the tornado forward motion (V_P) around the tornadic circulation radius. V_T can be estimated by averaging the maximum and minimum V_R on either side of the

Table 4. Summary of estimated wind speeds and EF-ratings for the 10 000 m² box with the greatest percent of tree falls using the ASCE WSE multi-tree DIs, the Canadian EF-scale, and the Godfrey and Peterson (2017) model. For the ASCE WSE wind speeds (Canadian EF-scale), the three numbers represent the below normal (lower-bound), normal (expected), and above normal (upper-bound) 3-s, 10-m AGL maximum wind gust values. For the Godfrey and Peterson estimate, the two numbers are estimated from their Fig. 7 based on the lower and upper 95% confidence interval.

Method	Monroe Tornado			Sterlington Tornado		
	Applicable Tree DI/DOD	Estimated Wind Speed Range (mph)	EF-Rating Range	Applicable Tree DI/DOD	Estimated Wind Speed Range (mph)	EF-Rating Range
ASCE WSE multi-tree DI	≥75% of large trees snapped or uprooted	120–145–170	EF2-EF4	≥75% of large trees snapped or uprooted	120–145–170	EF2-EF4
Canadian EF-scale	More than 80% of mature trees snapped and/or uprooted	118–146–170	EF2-EF4	More than 80% of mature trees snapped and/or uprooted	118–146–170	EF2-EF4
Godfrey and Peterson (2017)	84% of tree falls in a 100-m × 100-m plot	140–174	EF3-EF4	100% of tree falls in a 100-m × 100-m plot	212–224	EF5

tornadic circulation at the lowest elevation angle:

$$V_T = \frac{\text{maximum } V_R - \text{minimum } V_R}{2} \quad (1)$$

V_p was estimated for each scan by averaging the motion of the V_R couplet centroid position between successive radar scans. Across the ~10-min lifecycle of the Monroe tornado, its V_p ranged from 20 to 24 m s⁻¹. Figure 16 shows an example of the evaluation process as the circulation neared the KMLU ASOS site. The maximum ground-relative tornadic wind speed ($V_{G,max}$) using this method is presented in Table 6 (Radar-1 column) and the Fig. 16 animation. The estimated wind speeds ranged from 91 to 132 mph (weak EF-1 to almost EF-3 intensity) during the tornado’s lifecycle.

Another method of estimating tornado intensity from radar, and one that is easier to determine in a near real-time operational setting, is using the simulated tornado probabilities and intensities from Cohen et al. (2018) and conditional EF-rating probabilities from Elsner and Schroder (2019). From Cohen et al. (2018), the best predictors for tornado probability are V_{ROT} (kts), circulation diameter (DIST; n mi), a subjective clear or tight circulation designation (CT), and effective-layer significant tornado parameter (STP). Similarly, the best predictors for simulated tornado intensity are height of circulation above radar level (ARL; ft), V_{ROT} , STP, and whether or not a tornadic debris signature (TDS ;

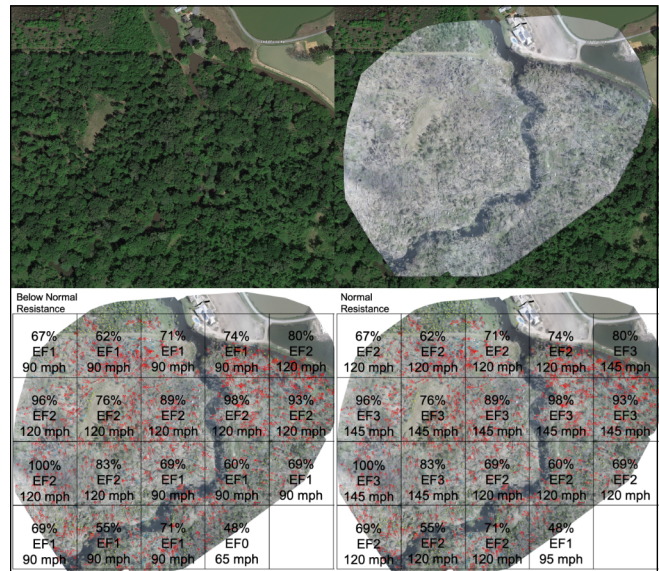


Figure 15. Similar to Fig. 14 but for a wooded area in the path of the Sterlington tornado.

Ryzhkov et al. 2005; Schultz et al. 2012a,b; Van Den Broeke and Jauernic 2014) is present. These inputs were determined for each KULM volume, except for STP, which was estimated from the 00-hr RAP sounding initialized at 16 UTC for KMLU. The results from the simulated tornado and EF-rating probability model are derived from a web-based tool developed by Burg (2020) that employs these methods. Estimated

Table 5. Damage survey information by EF-rating. Total area by EF-rating is measured in square kilometers and percent area by EF-rating is measured as a ratio of area by EF-rating and total area of the damage path (i.e., EF0 total area). Percent area for EF0 is calculated as the remaining total percentage of damage path after the determination of percent area for EF1–EF3 (i.e., $EF0 = 100 - (EF1 + EF2 + EF3)$).

EF-Rating	Damage Survey					
	NWS		ULM		Combined	
	Total Area (km ²)	Percent Area (%)	Total Area (km ²)	Percent Area (%)	Total Area (km ²)	Percent Area (%)
EF0	3.64	55.07	3.73	47.03	4.75	42.38
EF1	1.54	42.43	1.91	51.13	2.59	54.58
EF2	.089	2.48	.068	1.82	.12	3.02
EF3	.0006	.02	.0009	.02	.0012	.02

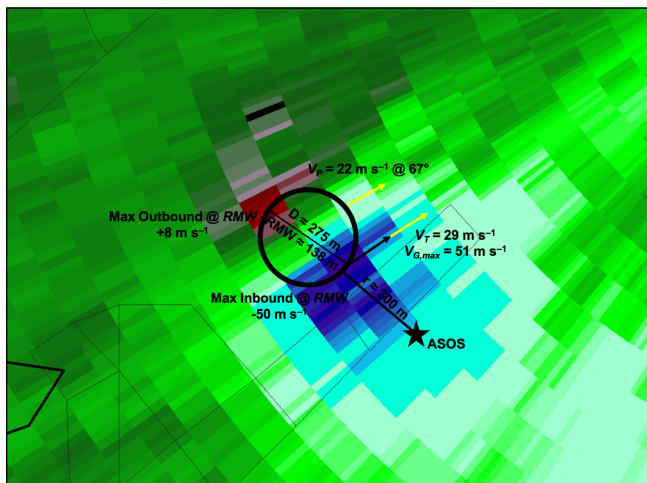


Figure 16. KULM radial velocity valid 1646 UTC 12 April 2020 during the tornadic circulation's closest approach to the KMLU ASOS (black star). The bold circle represents the circulation's RMW with a radius of approximately 138 m. The maximum inbound (outbound) radial velocity at the RMW is -50 m s^{-1} ($+8 \text{ m s}^{-1}$). The distance from the RMW to the ASOS (r) is approximately 300 m. The yellow vector represents the circulation's forward motion (V_P) and the black vector represents the rotational velocity (V_T) of the circulation. The maximum ground-relative speed in the circulation ($V_{G,max}$) is found through a vector addition of V_P and V_T . The black polygon at the left edge of the figure is the end of the surveyed tornado track. Click the image for an animation of radial velocity valid 1635–1645 UTC with $V_{G,max}$ and several damage survey points annotated.

wind speeds using this method (Radar-2 column in Table 6) ranged from 99 to 115 mph (strong EF-1 to weak EF-2 intensity) during the tornado's lifecycle.

The two methods yield similar wind speed estimates and corresponding maximum EF-ratings for each radar volume. The average wind speed difference between the two methods was approximately 7 mph. There were three volume times (1636, 1638, and 1645 UTC) where a ≥ 10 mph difference in wind speed was found. For each of those, the Radar-1 method gave a higher estimate. The two methods yielded a different EF-rating for two volumes (1640 and 1644 UTC), even though the estimated wind speed difference at both times was <10 mph. The conditional EF-rating probability indicated EF-1 intensity was $\geq 50\%$ likely for 8 of the 10 analyzed volume scans. EF-2 was the most likely rating at 1638 UTC at 40% probability, and EF-1 was the most likely rating at 1645 UTC at 42% probability. However, the conditional probabilities did not always correspond well to the radar derived wind estimates, occasionally suggesting a lower intensity than the radar data.

The center of the KULM V_{ROT} signature moved within 300 m of the KMLU ASOS site (Fig. 16), which measured a peak 10-m wind gust of 30.8 m s^{-1} (69 mph) at 1646 UTC. The official damage survey indicated the tornado track ended about 1 km west of the ASOS site, but it is possible the tornado continued further east for at least another 1–1.5 km; points to the east were over the airport runway with no damage indicators present. Near the end of the runway a patch of trees was undisturbed, indicating the tornado had most likely

Table 6. Radar estimated maximum tornado wind speeds and corresponding EF-rating for each KULM volume scan during the Monroe tornado based on traditional radar estimates (Radar-1) and the Cohen et al. (2018) method (Radar-2). The conditional EF-rating probabilities are based on Elsner and Schroder (2019). Also provided are the maximum EF-rating from damage surveys near these volume scan times.

Time (UTC)	Radar-1 (mph)	Radar-2 (mph)	EF0 Prob	EF1 Prob	EF2 Prob	EF3 Prob	EF4/5 Prob	NWS Rating	ULM Rating
16:35:28	101 (EF1)	106 (EF1)	14	57	22	6	1	EF1	EF1
16:36:29	121 (EF2)	111 (EF1)	9	50	30	9	2	EF1	EF1
16:37:30	120 (EF2)	115 (EF2)	6	43	35	13	3	EF2	EF2
16:38:32	132 (EF2)	119 (EF2)	4	33	40	19	4	EF1	EF2
16:39:33	105 (EF1)	107 (EF1)	12	56	24	7	1	EF2	EF2
16:40:34	114 (EF2)	108 (EF1)	11	54	26	7	1	EF2	EF2
16:41:36	91 (EF1)	99 (EF1)	26	58	13	3	1	EF1	EF2
16:42:37	103 (EF1)	105 (EF1)	15	58	13	3	1	EF2	EF2
16:43:38	103 (EF1)	107 (EF1)	12	56	24	7	1	EF1	EF2
16:44:39	116 (EF2)	109 (EF1)	10	53	28	8	2	EF1	EF1
16:45:41	127 (EF2)	115 (EF2)	6	42	36	14	3	EF2	EF2

dissipated by this time. Assuming a surface circulation was still present, the ASOS wind gust offers an opportunity to compare a near surface wind measurement in or near the tornado with the radar data. Here a radially dependent wind profile is applied assuming a modified Rankine profile with solid body rotation of the following form (Wurman and Alexander 2005):

$$V_G(r) = VG \times r'/_{RMW} \text{ for } r \leq RMW \quad (2)$$

$$V_G(r) = VG \times (RMW/r)^a \text{ for } r > RMW \quad (3)$$

where RMW is the radius of maximum winds, r is the distance from the RMW , and a is an exponential decay factor of 0.6. The RMW based on the maximum inbound and outbound V_R was 138 m, and the ASOS

site was approximately 300 m from the RMW . The $V_{G,max}$ at the RMW , based on the vector addition of V_T and V_P , was estimated at 51 m s^{-1} (114 mph). This provides a radar estimated speed at r of approximately 32 m s^{-1} (72 mph), close to that observed at the ASOS site.

Maximum TDS height has been shown to have some correlation to tornado intensity (Van Den Broeke and Jauernic 2014; Entremont and Lamb 2015), and a strong multivariate correlation exists between maximum TDS height, maximum V_{ROT} , and maximum tornado intensity (Emmerson et al. 2019). Unfortunately, the KULM scanning strategy did not allow for this type of investigation. However, the Shreveport WSR-88D (KSHV) data indicates the Monroe tornado lofted debris to approximately 4.2 to 4.6 km AGL (Fig. 17), which when combined with a

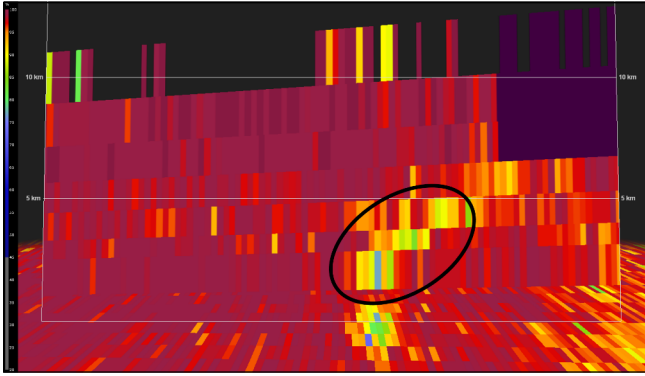


Figure 17. Vertical cross section of correlation coefficient (CC) from the Shreveport, LA WSR-88D taken through the tornadic debris signature of the Monroe EF-3 tornado near 1643 UTC. The circled area indicates the region of likely tornadic debris lofted to near 5 km AGL.

maximum V_{ROT} from KULM of approximately 36 m s^{-1} , suggests a peak intensity in the upper-end EF-2 to low-end EF-3 range. This corresponds well with the other radar-based intensity estimates.

5. Casualty modeling

Casualties are perhaps the most important tornado impact from a human ecology perspective. Some previous research on casualties is centered on the number or location of casualties (Grazulis 1990; Ashley 2007; Fricker et al. 2017). Other previous research is concerned with the prediction of casualties through an understanding of outside factors that play a role in a casualty event (Simmons and Sutter 2008, 2011; Lim et al. 2017; Fricker et al. 2017; Elsner et al. 2018; Fricker and Elsner 2019). Given the intensity of damage found within the path of the Monroe tornado, we would most likely expect some number of casualties. Formal surveys, however, found that zero casualties were directly attributable to the Monroe tornado, which suggests that some combination of accurate forecasting, warning response, and/or other unknown factors occurred. To measure just how successful this event was from a human impacts standpoint, we use regression analysis and prediction models (Fricker et al. 2017; Elsner et al. 2018; Fricker and Elsner 2019) seen in recent work to establish how many casualties, on average, we would expect to have in the Monroe tornado.

More specifically, here we apply estimates of tornado power, population density, mobile homes, and

year, month, and day of occurrence to predict how many casualties, on average, we would expect to have in the Monroe tornado. Formally, the model is given by

$$\begin{aligned} \ln(C) = & \ln(B_0) + B_P \ln(P) + B_E \ln(E) + \\ & B_{P \times E} [\ln(P) \times \ln(E)] + B_Y Y + B_{MH} MH + \\ & B_{MO} (1|MO) + B_{HR} (1|HR) \end{aligned} \quad (4)$$

where P is the population density in people per square kilometer, E is energy dissipation in watts (power), Y is the year of occurrence, MH is the estimated number of mobile homes, and MO and HR are the month and hour of occurrence, respectively (Fricker and Elsner 2019).

Unique to this modeling framework is the inclusion of tornado power, which is estimated as the product of tornado path area and the cube of the wind field. The wind field is a weighted average of the midpoint wind speed from the corresponding EF rating, where the weights are the fraction of damage path area by EF rating (Fricker et al. 2014). Because fractions of damage path area are not available in the historic record, previous work has relied on the use of the United States Nuclear Regulatory Commission (NRC) model for fractions (Ramsdell and Rishel 2007). Unlike the historic record, here we have a detailed tornado damage footprint, which allows us to apply the same method using the fractions of damage path area by EF rating found in the ULM survey. When compared to the NRC model, the ULM damage path footprint has a much larger percentage of EF-1 damage, much smaller percentages of EF-2 and EF-3 damage, and a slightly smaller percentage of EF-0 damage, resulting in a lower estimate of tornado power relative to the historic climatology.

Estimates of population density and the number of mobile homes were made using a dasymetric method outlined in Fricker (2020a). The procedure can be thought of as a spatial apportionment of Census information. Here, 2019 American Community Survey 5-year estimates are used as the underlying demographic information and the ULM damage path footprint is chosen as the tornado damage path. Using a ratio of the fraction of the tornado path that occurs within a census tract and the total area of the census tract, weighted estimates of population and mobile homes are made for each fraction of the tornado path and added together for the entirety of the footprint. Population density is estimated by dividing the estimated total population within the tornado path by the total area of the tornado path.

Once fitted, the model suggests that, on average, we would expect 19 total casualties in the Monroe EF-3 tornado. As mentioned above, formal damage surveys found that zero casualties were directly attributable to the tornado, which indicates a significant difference in the expected and observed human impacts of this tornado. As a means of evaluating the economic savings of reduced casualties we apply the value of statistical life (VSL) to the expected casualty numbers. Fricker (2020b) finds that one fatality has occurred for every 14 injuries in casualty-producing tornadoes over the period 1995-2016. Thus, we assign one estimated fatality and 18 estimated injuries as the most likely casualty scenario for the Monroe EF-3 tornado. Using the injury-type fraction by EF-rating and building type (Table 8 in Cho and Kurdzo 2019), we further assign 10 injuries as treat and release and 8 injuries as hospitalized. When applied to casualty cost by type (Table 7 in Cho and Kurdzo 2019), the VSL of the expected casualty counts in the Monroe EF-3 tornado amounts to \$38.74M with \$10.8M from the expected fatality, \$5.06M from the expected treat and release injuries, and \$22.88M from the expected hospitalized injuries.

6. Discussion & conclusions

It has been hypothesized that the near-storm QLCS environment can evolve quickly from one that is unfavorable for tornadoes to one that is favorable in narrow mesoscale regions where the low-level vertical wind shear maximizes and boundary layer instability increases. That appears to have been the case here; low-level shear rapidly increased in the near-storm environment of the QLCS, and the boundary layer became less stable, perhaps even undergoing rapid destabilization, as the QLCS approached. Recent numerical studies have also suggested that as low-level hodographs become longer and/or more curved ahead of QLCSs (i.e., greater amounts of low-level SRH), there is a greater chance for stronger and longer-lived vortices (Marion and Trapp 2021). The 0–1-km SRH reaching a mesoscale maximum in northeastern Louisiana might explain the stronger tornadoes in this region compared to weaker tornadoes along the rest of the QLCS path. Even though this is just a single case, these findings are compatible with hypotheses that will be further explored in the NSF and NOAA funded Propagation, Evolution, and Rotation in Linear Storms (PERiLS; <https://www.nssl.noaa.gov/projects/perils/>)

field project that began March 2022 in the SE United States.

Tornado intensity estimates were provided using two different radar methods, traditional damage surveys conducted by NWS Shreveport and ULM personnel, and estimates based on multiple tree falls. Even though this paper maps intensity estimates using these methods to a corresponding EF-rating, the radar and multiple tree fall methods are not part of the current operational EF-scale. Regardless, the intensity estimates paint a similar picture throughout the lifecycle of the Monroe tornado, with a few notable exceptions. Differences between the official NWS Shreveport damage survey and the survey compiled by ULM personnel are small (Table 5) and mainly arise for two reasons: (1) ULM personnel inspected each structure within and near the path of the tornado where aerial imagery was available¹, and (2) NWS Shreveport personnel were unable to safely survey some locations by ground. One such location was a wooded area along the path where the tree-fall analysis (Fig. 14) suggested EF-2 intensity at a minimum. The tree-fall intensity estimate is a better match with the radar estimates near this location (1638 UTC in Table 5). In three instances, the aerial survey showed residential homes with a significant loss of roof material and/or large sections of the roof missing at the rear of the structure; these structures were rated as EF-2 intensity in ULM's survey, but were originally listed as EF-1 in the NWS survey. Radar estimates suggested upper-end EF-1 to EF-2 damage near one of the structures, while suggesting EF-1 intensity near the others. For one home, the build quality of the structure and roof material was questioned during the NWS ground survey, so the higher EF rating was difficult to justify. For the other homes, the full scope of the damage was not visible during the ground survey, though NWS personnel indicated the build quality of these structures also would have been questioned. Regardless, not being able to physically inspect build quality is a limitation of only performing an aerial survey.

Similarly, the Sterlington, Louisiana tornado survey was improved by the addition of an aerial survey of a wooded area impacted early in its damage path. This tornado was originally rated EF-2 by the NWS, but was later upgraded to EF-3 intensity after further survey analysis. The aerial survey increased NWS

¹ There are some areas the aerial survey was unable to view because of UAS flight restrictions imposed by the FAA.

Shreveport's confidence in the rating upgrade (B. Bryant and C. Woodrum, NWS Shreveport, 2021, personal communication). With the likely inclusion of new damage indicators in a future update to the EF-scale, such as the multiple tree-fall damage indicator, being able to conduct a complete survey (i.e., both ground AND aerial) will be an important consideration for NWS offices moving forward to capture more accurate tornado intensity estimates.

The radar intensity estimates are limited by (1) volume scan time (here ~60 s), (2) inability to provide an estimate of 3-s gust at 10-m AGL, and (3) radar sampling issues (e.g., Wood and Brown 1997) that may not capture the true speeds across the vortex couplet. Past studies have shown that tornado wind speeds near the ground are similar, or even slightly greater, than those winds observed from 50–200 m AGL (e.g., Wurman et al. 2021). It is also important to consider that Doppler radars provide statistical estimates of the radial component of the reflectivity-weighted motion of scatterers in a sample volume, the size of which is based on radar operating specifications and distance from the radar. Although the radar intensity estimates compare favorably to the damage survey ratings near those volume scan times (Table 5), the radar missed or was unable to resolve the strongest tornadic winds considering there were a few areas of extreme localized damage. The NWS Shreveport damage survey speculated an intense sub-vortex may have been responsible for the EF-3 damage to one single family home on Orchid Drive in Monroe (Fig. 13c). The radar estimates near this location maximized at EF-1 intensity, which would lend support to their hypothesis. Even though there was a mismatch in EF rating, the radar estimates do show a wind speed increase leading up to the EF-3 damage point, indicating a strengthening vortex at this time. This case shows a reasonable correspondence between both radar methods, and ultimately what was found through ground and aerial damage surveys.

The initial tornado warning for the Monroe tornado was issued at 1633 UTC, and the tornado developed at 1636 UTC. Although the initial warning had ~3 minutes of lead time, this was 9–10 minutes before the tornado moved through the more densely populated urban center. It is important to appreciate just how quickly the tornadic circulation developed; the warning was issued nearly coincident with the first signs of a slightly stronger KULM V_{ROT} signature. One issue with KULM described in Murphy et al. (2019) is volume scans are

not available in GR2A until after the entire volume completes, which adds a 30-to-60 s delay on data delivery. However, without the improved low-level coverage and fast volume scan updates provided by KULM, a warning may not have been issued until damage reports were received (B. Bryant and C. Woodrum, NWS Shreveport, 2021, personal communication). The improved coverage and subjective value of KULM was previously described in Murphy et al. (2019), but here we provided a better value estimate based on expected casualty counts (see §5). And whereas it is impossible to link 19 expected casualties not occurring because of KULM, it is likely that there would have been an increased chance of casualties if the tornado warning had a shorter lead time, which may have occurred without KULM coverage. It is reasonable to assume that KULM played some role in the nearly \$39M of casualty loss savings.

This case also demonstrates the immense value of in-depth mesoscale analysis during nowcasting and warning operations. All data sources indicated tornadoes occurred in regions where the low-level shear was maximized, and where the QLCS became better aligned with the 0–3-km shear vector. More generally, tornadic development was supported where both the 3IM criteria were met and where large values of 0–1-km SRH were present. These are parameters and methods that can be analyzed in real time during warning operations to further increase confidence. The Monroe tornado development could have been anticipated by 1630 UTC (3 minutes before the initial warning), as this was when a weak V_{ROT} signature first developed, which by itself does not warrant action. However, the weak V_{ROT} , coupled with prior tornadic activity, the 3IM criteria being met, a strengthening mesovortex north of a Z_H surge, and a local maximum in low-level SRH, all call for that portion of the QLCS to be closely monitored for quick warning issuance.

Acknowledgments. A National Science Foundation Rapid Response Research Grant, AGS-2030098, provided funding for the UAS flights, data preservation, and preliminary research. Subsequent research was supported by the VORTEX-USA program within the NOAA/OAR Weather Program Office under Award No. NA21OAR4590324. Paul Karlowitz and Stephanie Robinson from the ULM UAS Management program performed the UAS flights of the tornado track. Drs. Chris Peterson (University of Georgia) and Chris Godfrey (University North Carolina at Asheville)

provided information vital to the tornado tree fall intensity estimates. Conversations with Dr. Tony Lyza (CIWRO/OU/NSSL) were helpful in interpretation of damage and radar data. Dr. Patrick Marsh (SPC) provided the SFCOA gridded data used in the SPC Mesoanalysis. Daniel Lamb (NWS Jackson, Mississippi) provided a review that improved an initial version of the manuscript. Comments and suggestions from three anonymous reviewers greatly improved the original manuscript. The MetPy, SHARPy, and gempakIO Python libraries were utilized for data analysis. Any statements, findings, conclusions, and/or recommendations provided in this paper are those of the authors and do not necessarily reflect the views of NOAA or the United States Department of Commerce.

REFERENCES

- Anderson-Frey, A. K., Y. P. Richardson, A. R. Dean, R. L. Thompson, and B. T. Smith, 2019: Characteristics of tornado events and warnings in the southeastern United States. *Wea. Forecasting*, **34**, 1017–1034, [CrossRef](#).
- Ashley, W. S., 2007: Spatial and temporal analysis of tornado fatalities in the United States: 1880–2005. *Wea. Forecasting*, **22**, 1214–1228, [CrossRef](#).
- Ashley, W. S., A. M. Haberlie, and J. Strohm, 2019: A climatology of quasi-linear convective systems and their hazards in the United States. *Wea. Forecasting*, **34**, 1605–1631, [CrossRef](#).
- Atkins, N. T., and M. St. Laurent, 2009: Bow echo mesovortices. Part I: Processes that influence their damaging potential. *Mon. Wea. Rev.*, **137**, 1497–1513, [CrossRef](#).
- Bentley, E. S., R. L. Thompson, B. R. Bowers, J. G. Gibbs, and S. E. Nelson, 2021: An analysis of 2016–18 tornadoes and National Weather Service tornado warnings across the contiguous United States. *Wea. Forecasting*, **36**, 1909–1924, [CrossRef](#).
- Blumberg, W. G., Halbert, K. T., Supinie, T. A., Marsh, P. T., Thompson, R. L., and Hart, J. A., 2017: SHARPy: An open-source sounding analysis toolkit for the atmospheric sciences. *Bull. Amer. Meteor. Soc.*, **98**(8), 1625–1636, [CrossRef](#).
- Bodine, D. J., R. D. Palmer, and G. Zhang, 2014: Dual-wavelength polarimetric radar analyses of tornadic debris signatures. *J. Appl. Meteor. Climatol.*, **53**, 242–261, [CrossRef](#).
- Brotzge, J. A., S. E. Nelson, R. L. Thompson, and B. T. Smith, 2013: Tornado probability of detection and lead time as a function of convective mode and environmental parameters. *Wea. Forecasting*, **28**, 1261–1276, [CrossRef](#).
- Burg, T., 2020: *Simulated Tornado Probability & Wind Speed*, [CrossRef](#).
- Cho, J. Y. N. and J. M. Kurdzo, 2019: Weather radar network benefit model for tornadoes. *J. Appl. Meteor. Climatol.*, **58** (5), 971–987, [CrossRef](#).
- Coffer, B. E., M. D. Parker, R. L. Thompson, B. T. Smith, and R. E. Jewell, 2019: Using near-ground storm relative helicity in supercell tornado forecasting. *Wea. Forecasting*, **34**, 1417–1435, [CrossRef](#).
- Coffer, B. E., M. Taszarek, and M. D. Parker, 2020: Near-ground wind profiles of tornadic and nontornadic environments in the United States and Europe from ERA5 reanalyses. *Wea. Forecasting*, **35**, 2621–2638, [CrossRef](#).
- Cohen, A. E., J. B. Cohen, R. L. Thompson, and B. T. Smith, 2018: Simulating tornado probability and tornado wind speed based on statistical models. *Wea. Forecasting*, **33**, 1099–1108, [CrossRef](#).
- Elsner, J. B., and Z. Schroder, 2019: Tornado damage ratings estimated with cumulative logistic regression. *J. Appl. Meteor. Climatol.*, **58**, 2733–2741, [CrossRef](#).
- Elsner, J. B., T. Fricker, and W. D. Berry, 2018: A model for United States tornado casualties involving interaction between damage path estimates of population density and energy dissipation. *J. Appl. Meteor. Climatol.*, **57**, 2035–2046, [CrossRef](#).
- Emmerson, S. W., S. E. Nelson, and A. K. Baker, 2019: A Comprehensive Analysis of Tornadic Debris Signatures Associated with Significant Tornadoes from 2010–2017. *99th American Meteorological Society Annual Meeting*, Phoenix, AZ, Amer. Meteor. Soc., PS210, [CrossRef](#).
- Entremont, C., and J. D. Lamb, 2015: The Relationship between Tornadic Debris Signature Height and Tornado Intensity. *95th American Meteorological Society Annual Meeting*, Phoenix, AZ, Amer. Meteor. Soc., P452 [Available at <https://ams.confex.com/ams/95Annual/webprogram/Paper268874.html>].
- Environment Canada, cited 2022: Enhanced Fujita scale damage indicators and degrees of damage, chapter 27: C-2 Trees (C-T). [Available online <https://www.canada.ca/en/environment-climate-change/services/seasonal-weather-hazards/publications/enhanced-fujita-scale-damage-indicators/chapter-27.html>]
- Fricker, T., 2020a: Tornado-level estimates of socioeconomic and demographic variables. *Natural Hazards Review*, **21**, 04020018, [CrossRef](#).
- _____, 2020b: Evaluating tornado casualty rates in the United States. *Int. J. Disaster Risk Reduction*, **47**, 101535, [CrossRef](#).

- _____, and J. B. Elsner, 2019: Unusually devastating tornadoes in the United States: 1995–2016. *Annals of the American Association of Geographers*, **110**, 724–738, [CrossRef](#).
- _____, _____, P. Camp, and T. H. Jagger, 2014: Empirical estimates of kinetic energy from some recent U.S. tornadoes. *Geophys. Res. Lett.*, **41** (12), 4340–4346, [CrossRef](#).
- _____, _____, V. Mesev, and J.T. Jagger, 2017a: A dasymetric method to spatially apportion tornado casualty counts. *Geomatics, Natural Hazards and Risk*, **8** (2), 1768–1782, [CrossRef](#).
- _____, _____, and T. H. Jagger, 2017b: Population and energy elasticity of tornado casualties. *Geophysical Research Letters*, **44**, 3941–3949, [CrossRef](#).
- Gensini, V. A., C. Converse, W. S. Ashley, and M. Taszarek, 2021: Machine learning classification of significant tornadoes and hail in the United States using ERA5 proximity soundings. *Wea. Forecasting*, **36**, 2143–2160, [CrossRef](#).
- Gibbs, J. G., 2016: A skill assessment of techniques for real-time diagnosis and short-term prediction of tornado intensity using the WSR-88D. *J. Operational Meteor.*, **4** (13), 170–181, [CrossRef](#).
- _____, 2021: Evaluating precursor signals for QLCS tornado and higher impact straight-line wind events. *J. Operational Meteor.*, **9** (5), 62–75, [CrossRef](#).
- _____, and B. R. Bowers, 2019: Techniques and thresholds of significance for using WSR-88D velocity data to anticipate significant tornadoes. *J. Operational Meteor.*, **7** (9), 117–137, [CrossRef](#).
- Godfrey, C. M., and C. J. Peterson, 2017: Estimating enhanced Fujita scale levels based on forest damage severity. *Wea. Forecasting*, **32**, 243–252, [CrossRef](#).
- Grazulis, T. P., 1990: Significant Tornadoes, 1880–1989: Discussion and Analysis Significant Tornadoes, 1880–1989, Environmental Films.
- King, J. R., M. D. Parker, K. D. Sherburn, and G. M. Lackmann, 2017: Rapid evolution of cool season, low-CAPE severe thunderstorm environments. *Wea. Forecasting*, **32**, 763–779, [CrossRef](#).
- Kingfield, D. M. and J. G. LaDue, 2015: The relationship between automated low-level velocity calculations from the WSR-88D and maximum tornado intensity determined from damage surveys. *Wea. Forecasting*, **30**, 1125–1139, [CrossRef](#).
- Knupp, K. R., and Coauthors, 2014: Meteorological overview of the devastating 27 April 2011 tornado outbreak. *Bull. Amer. Meteor. Soc.*, **95**, 1041–1062, [CrossRef](#).
- LaDue, J. G., 2016: About the ASCE Tornado Wind Speed Estimation Standards Committee. *28th Conf. on Severe Local Storms*, Portland, OR, Amer. Meteor. Soc., 6B.1. [Available at ams.confex.com/ams/28SLS/webprogram/Paper300684.html]
- LaDue, J. G., and E. A. Mahoney, 2006: Implementing the New Enhanced Fujita Scale within the NWS. Preprints, *23rd Conf. on Severe Local Storms*, St. Louis, MO, Amer. Meteor. Soc., 5.5. [Available at ams.confex.com/ams/23SLS/webprogram/Paper115420.html]
- LaDue, J. G., J. Wurman, M. Levitan, F. T. Lombardo, C. D. Karstens, J. Robinson, and W. Coulbourne, 2018: Advances in development of the ASCE/SEI/AMS standard for wind speed estimation in tornadoes and other windstorms. *29th Conf. on Severe Local Storms*, Stowe, VT, Amer. Meteor. Soc., 29. [Available at ams.confex.com/ams/29SLS/meetingapp.cgi/Paper/348726]
- Lim, J., S. Loveridge, R. Shupp, and M. Skidmore, 2017: Double danger in the double wide: Dimensions of poverty, housing quality and tornado impacts. *Regional Science and Urban Economics*, **65**, 1–15, [CrossRef](#).
- Marion, G. R., and R. J. Trapp, 2021: Controls of quasi-linear convective system tornado intensity. *J. Atmos. Sci.*, **78**, 1189–1205, [CrossRef](#).
- Markowski, P. M., E. N. Rasmussen, and J. M. Straka, 1998: The occurrence of tornadoes in supercells interacting with boundaries during VORTEX-95. *Wea. Forecasting*, **13**, 852–859, [CrossRef](#).
- Murphy, T. A., C. Palmer, C. Entremont, and J. D. Lamb, 2019: Early operational successes of the University of Louisiana Monroe's Polarimetric S-band Doppler radar. *J. Operational Meteor.*, **7** (8), 105–116, [CrossRef](#).
- Päschke, E., R. Leinweber, and V. Lehmann, 2015: An assessment of the performance of a 1.5 μm Doppler lidar for operational vertical wind profiling based on a 1-year trial. *Atmos. Meas. Tech.*, **8**, 2251–2266, [CrossRef](#).
- Ramsdell Jr, J. V., and J. P. Rishel, 2007: "Tornado climatology of the contiguous United States" (Tech. Rep. Nos. NUREG/CR-4461, PNNL-15112). Richland, WA: Pacific Northwest National Laboratory, [CrossRef](#).
- Rasmussen, E. N., S. Richardson, J. M. Straka, P. M. Markowski, and D. O. Blanchard, 2000: The association of significant tornadoes with a baroclinic boundary on 2 June 1995. *Mon. Wea. Rev.*, **128**, 174–191, [CrossRef](#).
- Rotunno, R., J. B. Klemp, and M. L. Weisman, 1988: A theory for strong, long-lived squall lines. *J. Atmos. Sci.*, **45**, 463–485, [CrossRef](#).
- Ryzhkov, A. V., T. J. Schuur, D. W. Burgess, and D. S. Zrnić, 2005: Polarimetric tornado detection. *J. Appl. Meteor.*, **44**, 557–570, [CrossRef](#).
- Schaumann, J. S., and R. W. Przybylinski, 2012: Operational Application of 0–3 km Bulk Shear Vectors in Assessing QLCS Mesovortex and Tornado Potential. Preprints, *26th Conf. on Severe Local Storms*, Nashville, TN, Amer. Meteor. Soc., 9.10. [Available at <https://ams.confex.com/ams/26SLS/webprogram/Paper212008.html>]

- Schenkman, A. D., M. Xue, and A. Shapiro, 2012: Tornadogenesis in a Simulated Mesovortex within a Mesoscale Convective System. *J. Atmos. Sci.*, **69**, 3372–3390, [CrossRef](#).
- Schultz, C. J., and Coauthors, 2012a: Dual-polarization tornadic debris signatures Part I: Examples and utility in an operational setting. *Electronic J. Oper. Meteor.*, **13**, 120–137, [CrossRef](#).
- _____, and _____, 2012b: Dual-polarization tornadic debris signatures Part II: Comparisons and caveats. *Electronic J. Oper. Meteor.*, **13**, 138–150, [CrossRef](#).
- Sherburn, K. D. and M. D. Parker, 2014: Climatology and ingredients of significant severe convection in high-shear, low-CAPE environments. *Wea. Forecasting*, **29**, 854–877, [CrossRef](#).
- _____, _____, J. R. King, and G. M. Lackmann, 2016: Composite environments of severe and nonsevere high-shear, low-CAPE convective events. *Wea. Forecasting*, **31**, 1899–1927, [CrossRef](#).
- Simmons K. M., and D. Sutter, 2008: Tornado warnings, lead times, and tornado casualties: An empirical investigation. *Wea. Forecasting*, **23**, 246–258, [CrossRef](#).
- _____, and _____, 2011: Economic and Societal Impacts of Tornadoes. American Meteorological Society, Boston, pp. 1–8. [Available at <https://doi.org/10.1007/978-1-935704-02-7>].
- Smith, B. T., R. L. Thompson, J. S. Grams, C. Broyles, and H. E. Brooks, 2012: Convective modes for significant severe thunderstorms in the contiguous United States. Part I: Storm classification and climatology. *Wea. Forecasting*, **27**, 1114–1135, [CrossRef](#).
- _____, _____, A.R. Dean, and P.T. Marsh, 2015: Diagnosing the conditional probability of tornado damage rating using environmental and radar attributes. *Wea. Forecasting*, **30**, 914–932, [CrossRef](#).
- Tang, B., M. Vaughan, R. Lazear, K. Corbosiero, L. Bosart, T. Wasula, I. Lee, and K. Lipton, 2016: Topographic and boundary influences on the 22 May 2014 Duanesburg, New York, tornadic supercell. *Wea. Forecasting*, **31**, 107–127, [CrossRef](#).
- Thompson, R. L., B. T. Smith, J. S. Grams, A. R. Dean, and C. Broyles, 2012: Convective modes for significant severe thunderstorms in the contiguous United States. Part II: Supercell and QLCS tornado environments. *Wea. Forecasting*, **27**, 1136–1154, [CrossRef](#).
- _____, and Coauthors, 2017: Tornado damage rating probabilities derived from WSR-88D data. *Wea. Forecasting*, **32**, 1509–1528, [CrossRef](#).
- Toth, M., R. J. Trapp, J. Wurman, and K. A. Kosiba, 2013: Comparison of mobile-radar measurements of tornado intensity with corresponding WSR-88D measurements. *Wea. Forecasting*, **28**, 418–426, [CrossRef](#).
- Trapp, R. J., and M. L. Weisman, 2003: Low-level vortices within squall lines and bow echoes: Part II. Their genesis and implications. *Mon. Wea. Rev.*, **131**, 2804–2823, [CrossRef](#).
- _____, S. A. Tessendorf, E. S. Godfrey, and H. E. Brooks, 2005: Tornadoes from squall lines and bow echoes. Part I: Climatological distribution. *Wea. Forecasting*, **20**, 23–34, [CrossRef](#).
- Van Den Broeke, M.S., 2017: Potential tornado warning improvement resulting from utilizing of the TDS in the warning decision process. *J. Operational Meteor.*, **5** (10), 121–133, [CrossRef](#).
- _____, and S. T. Jauernic, 2014: Spatial and temporal characteristics of polarimetric tornadic debris signatures. *J. Appl. Meteor. Climatol.*, **53**, 2217–2231, [CrossRef](#).
- Warning Decision Training Division, 2019: Three Ingredients Method, [CrossRef](#).
- Weisman, M. L., and R. J. Trapp, 2003: Low-level vortices within squall lines and bow echoes: Part I. Overview and dependence on environmental shear. *Mon. Wea. Rev.*, **131**, 2779–2803, [CrossRef](#).
- Wheatley, D. M., and R. J. Trapp, 2008: The effect of mesoscale heterogeneity on the genesis and structure of mesovortices within quasi-linear convective systems. *Mon. Wea. Rev.*, **136**, 4220–4241, [CrossRef](#).
- Wood, V. T., and R. A. Brown, 1997: Effects of radar sampling on single-Doppler velocity signatures of mesocyclones and tornadoes. *Wea. Forecasting*, **12**, 928–938, [CrossRef](#).
- Wurman, J., and C. R. Alexander, 2005: The 30 May 1998 Spencer, South Dakota, storm. Part II: Comparison of observed damage and radar-derived winds in the tornadoes. *Mon. Wea. Rev.*, **133**, 97–119, [CrossRef](#).
- _____, _____, P. Robinson, and Y. Richardson, 2007: Low-level winds in tornadoes and potential catastrophic tornado impacts in urban areas. *Bull. Amer. Meteor. Soc.*, **88**, 31–46, [CrossRef](#).
- _____, K. Kosiba, and P. Robinson, 2013: In situ, Doppler radar, and video observations of the interior structure of a tornado and the wind–damage relationship. *Bull. Amer. Meteor. Soc.*, **94**, 835–846, [CrossRef](#).
- _____, _____, T. White, and P. Robinson, 2021: Supercell tornadoes are much stronger and wider than damage-based ratings indicate. *Proc. Natl. Acad. Sci. USA*, **118**, e2021535118, [CrossRef](#).